Modern Physics Letters A Vol. 35, No. 25 (2020) 2030011 (21 pages) © World Scientific Publishing Company DOI: 10.1142/S0217732320300116



# Review of uncertainties in the cosmic supernova relic neutrino background

G. J. Mathews\* and L. Boccioli<sup>†</sup>

Center for Astrophysics, Department of Physics, University of Notre Dame, Notre Dame, IN 46556, USA \*gmathews@nd.edu $^{\dagger}lbocciol@nd.edu$ 

#### J. Hidaka

Mechanical Engineering Department, Meisei University, Tokyo 191-8506, Japan National Astronomical Observatory of Japan Tokyo, 181-8588, Japan jun.hidaka@meisei-u.ac.jp

#### T. Kajino

National Astronomical Observatory of Japan Tokyo, 181-8588, Japan International Research Center for Biq-Bang Cosmology and Element Genesis, and School of Physics, Beihang University, Beijing 100083, People's Republic of China Graduate School of Science, The University of Tokyo, Tokyo, 113-0033, Japan kajino@buaa.edu.cn; kajino@nao.ac.jp

> Received 19 July 2019 Revised 12 May 2020 Accepted 18 May 2020 Published 15 July 2020

We review the computation of and associated uncertainties in the current understanding of the relic neutrino background due to core-collapse supernovae, black hole formation and neutron star merger events. We consider the current status of uncertainties due to the nuclear equation of state (EoS), the progenitor masses, the source supernova neutrino spectrum, the cosmological star formation rate, the stellar initial mass function, neutrino oscillations, and neutrino self-interactions. We summarize the current viability of future neutrino detectors to distinguish the nuclear EoS and the temperature of supernova neutrinos via the detected relic supernova neutrino spectrum.

Keywords: Diffuse radiation; neutrinos; stars: formation, massive; supernovae: stars, supergiants.

2030011-1

PACS Nos.: 26.50.+x, 97.60.Bw, 97.60.Jd, 26.60.Kp

<sup>\*</sup>Corresponding author.

## 1. Introduction

For a number of years, there has been interest  $^{1-23}$  in the possibility of detecting the cosmic background due to supernova relic neutrinos (SRN). This is also referred to as the diffuse supernova neutrino background  $^5$  (DSNB). Although there are other contributions to the diffuse neutrino background from neutron star merger events (NSMs) associated with neutron star + neutron star binaries, or black hole + neutron star binaries,  $^{24-26}$  the dominant contribution to the diffuse neutrino background is from core-collapse supernovae (CCSNe).  $^{16}$ 

Massive stars ( $M \ge 8~M_{\odot}$ ) culminate their evolution as either a CCSNe or as a failed supernovae (fSNe) leading to a black hole remnant. In either case, such explosive events are expected to produce an intense flux of neutrinos with total energy of order  $\sim 10^{53}$  ergs emitted over an interval of  $\sim 10$  s for CCSNe or  $\sim 1$  s for fSNe.

Neutrinos are weakly interacting elementary particles, and therefore can emerge from within the interior of CCSNe, fSNe, and NSMs. As such, neutrinos can provide information regarding the physical processes that take place inside these explosive environments. The detection of this diffuse relic neutrino background and the associated energy spectra could provide information on neutrino properties such as flavor oscillations<sup>13,14</sup> and/or the neutrino temperatures produced in CCSNe explosions. <sup>16</sup> One may even be able to discern<sup>15</sup> the shock revival time from the detected spectrum of relic neutrinos. Moreover, these neutrino emission processes have continued over the history of the Galaxy. Hence, a detection of the SRN background will not only probe the physics of CCSNe, fSNe, and NSMs, but also the history of explosive events in the Galaxy, <sup>27</sup> as well as the cosmic expansion history itself. <sup>22</sup> The possible interaction of neutrinos with the DSNB also constrains beyond standard-model physics. <sup>28</sup>

The prospect for detecting the SRN background in the near future seems possible due to plans  $^{29,30}$  for a next generation Hyper-Kamiokande detector with a megaton of pure water laden with 0.1-0.2% GdCl $_3$  to enhance the neutron tagging efficiency and reduce the background. Moreover, results from the Super-Kamiokande collaboration already place some marginal limits on the total neutrino energies and temperatures from the background spectrum of SRN. The possibility of a liquid scintillation detector has also been discussed.

However, as analyzed in a number of works (e.g. Refs. 16–19), theoretical predictions of the detection rate of SRN are still subject to a number of uncertainties. These uncertainties include the time dependence of the stellar initial mass function (IMF), the star formation rate (SFR) and/or SN rate, the roles of neutrino oscillations and/or neutrino self-interaction, and the spectral energy distributions (SEDs) of the three flavors of SN neutrinos. These in turn depend upon the explosion mechanism, the equation of state (EoS) for proto-neutron stars, and whether the final remnant is a neutron star or black hole. In this review, we summarize the current status of some of these uncertainties. In particular, we highlight the new

trends toward decreasing uncertainty due to the EoS and the SN neutrino spectrum and luminosity.

## 2. The Relic Neutrino Background

The presently arriving cosmic diffuse neutrino flux spectrum  $dN_{\nu}/dE_{\nu}$  can be derived  $^{1,33,34}$  from an integral over the cosmic redshift z of the neutrinos emitted per event (SN or NSM) and the cosmic event rate per redshift per comoving volume  $(R_{\rm SN}(z))$  and  $R_{\rm NSM}(z)$ :

$$\frac{dN_{\nu}}{dE_{\nu}} = \frac{c}{H_0} \int_0^{z_{\text{max}}} \left[ R_{\text{SN}}(z) \frac{dN_{\nu}^{\text{SN}}(E_{\nu}')}{dE_{\nu}'} + R_{\text{NSM}}(z) \frac{dN_{\nu}^{\text{NSM}}(E_{\nu}')}{dE_{\nu}'} \right] \times \frac{dz}{\sqrt{\Omega_m (1+z)^3 + \Omega_{\Lambda}}}, \tag{1}$$

where  $z_{\rm max} \approx 5$  is the redshift at which star formation begins. The various contributions to  $R_{\rm SN}$  are described below, while  $R_{\rm NSM}$  is the corresponding number of NSM events. The quantities  $dN_{\nu}^{\rm SN}(E'_{\nu})/dE'_{\nu}$  and  $dN_{\nu}^{\rm NSM}(E'_{\nu})/dE'_{\nu}$  are the emitted neutrino spectra at the various sources, where the energy  $E'_{\nu} = (1+z)E_{\nu}$  is the energy at emission, while  $E_{\nu}$  is the redshifted energy to be observed in the detector. In addition to integrating over the range of progenitor models to determine  $R_{\rm SN}$  for normal CCSNe, one should add<sup>16</sup> the neutrino emission from ONeMg electron-capture SNe, the neutrino emission from the collapse of massive stars that form black holes, and the contribution from NSMs. The contribution from NSMs is small but potentially interesting. The reader is referred to Refs. 24 and 25 for discussions of this possibility. For the remainder of this review, we will only consider contributions from various classes of SNe or black hole formation.

Figure 1 from Ref. 16 illustrates the arriving neutrino flux from different SN sources as labelled. This figure is for the case of no neutrino oscillations (Case III as defined below). We next review the various factors in Eq. (1) in detail.

## 2.1. Core-collapse supernova rate $R_{\rm SN}$

The core-collapse supernova rate  $R_{\rm SN}$  can be determined from the total SFR [i.e. total mass in stars formed per year per comoving volume], if one determines the fraction of total stars that produce each observable class of SNe or other sources. The general form for the SN rate at a given redshift z is related to the SFR  $\psi_*(z)$  and the IMF  $\phi(M)$ .

$$R_{\rm SN}(z) = \psi_*(z) \times \frac{\int_{\rm min}^{\rm max} dM \, \phi(M)}{\int_{M_{\rm min}}^{M_{\rm max}} dM \, M\phi(M)},\tag{2}$$

where min and max denote the range of progenitors for SNe. As described below this may be a sum of segments that lead to CCSNe or fSNE separately. The quantities  $M_{\rm min}$  and  $M_{\rm max}$  refer to the range over all stars formed.

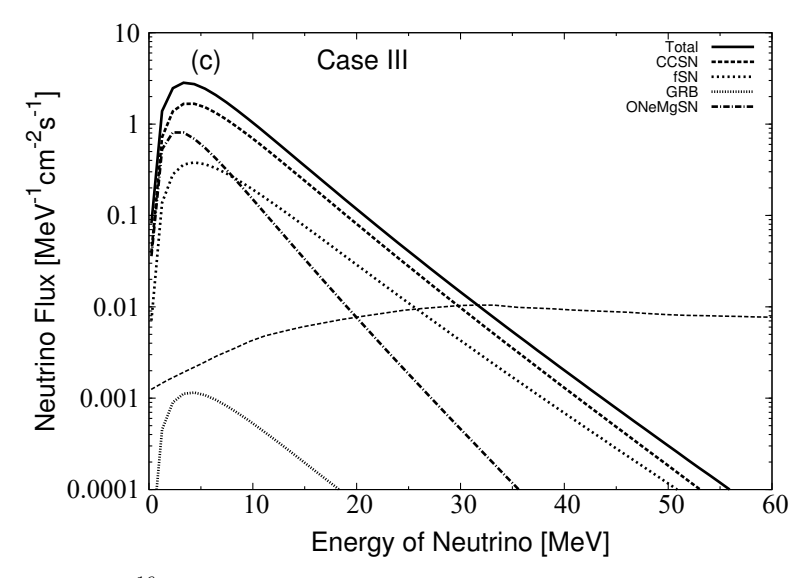


Fig. 1. Illustration<sup>16</sup> of the relative contributions to the total predicted SRN flux spectrum (solid line) from different sources in the case of no neutrino oscillations (Case III). These are CCSNe (short-dashed line); ONeMg (dot-dashed line); fSNe (dotted line); and collapsar GRBs (small dotted line). The background due to atmospheric neutrinos is also indicated as a short-dashed line.

It is often assumed<sup>35</sup> that all massive progenitors from 8 to 40  $M_{\odot}$  lead to visible SNe. The higher end of this mass range corresponds to SNIb,c, while the lower end corresponds to normal SNII.

In Ref. 16, however, it was pointed out contributions from both normal core-collapse SNII and SNIb,c should be considered separately, along with the possibility of fSNe forming a black hole and dim ONeMg supernovae in the low-mass end. The SNIb,c events accounts for about  $\sim 25 \pm 10\%$  of observed CCSN rate at redshift near  $z=0.^{36}$  Hence, for the total observed core-collapse SN rate one can write:

$$R_{\rm SN}(z) = R_{\rm SNII}(z) + R_{\rm SNIb,c}(z). \tag{3}$$

Nevertheless, there is large uncertainty in the mass ranges of CCSNe and the degree to which progenitors have experienced mass loss such that the true initial progenitor mass could be greater.

Observational evidence for the mass of SN progenitors has been obtained  $^{36,37}$  by comparing sky images of nearby SNe before and after explosion. This suggests that the maximum mass of the red supergiant progenitors of core-collapse SNe may be as small as  $16.5~M_{\odot}$ . This is the so-called red supergiant (RSG) problem.  $^{36,37}$  A subsequent study,  $^{38}$  however, suggested that this value could be as much as  $18~M_{\odot}$ . A similar range was deduced in Ref. 39 who argued that this limit is closely related to the transition from convective to radiative transfer during the central carbon-burning phase. Hence, 16.5 to  $18~M_{\odot}$  was adopted in Ref. 17 as a reasonable range of the uncertainty in the lower mass limit for fSNe.

It is also believed<sup>40</sup> that initial progenitor stars in the mass range of 8–10  $M_{\odot}$  collapse as an electron degenerate ONeMg core and do not produce bright SNe. Hence, one should consider a lower limit to the progenitor of normal CCSNe of 10  $M_{\odot}$  when allowing for the possibility of ONeMg SNe.

Regarding SNIb,c, although it is known<sup>36</sup> that they are associated with massive star forming regions, there is some ambiguity as to their progenitors. There are two theoretical possibilities. References 40 and 41 have studied the possibility that massive stars ( $M \sim 25$ –100  $M_{\odot}$ ) can shed their outer envelope by radiative-driven winds leading to bright SNIb,c explosions. This source for SNIb,c was adopted in Ref. 35 by assuming that all stars with ( $M \sim (25$ –40)  $M_{\odot}$ ) explode as SNIb,c, while Ref. 27 adopted a range of 25–50  $M_{\odot}$  for SNIb,c. Changing the upper mass limit from 40  $M_{\odot}$  to 50  $M_{\odot}$ , however, makes little difference ( $\sim 1\%$ ) in the inferred total CCSN rate.<sup>16</sup>

Theoretically, however, this single massive-star paradigm does not occur as visible SNeIb,c until well above solar metallicity. At lower metallicity most massive stars with  $M>25~M_{\odot}$  collapse as fSNe with black hole remnants. Hence, this mechanism is not likely to contribute to the observed SNIb,c rate at higher redshifts. On the other hand, it has been estimated that 15–30% of massive stars up to  $\sim 40~M_{\odot}$  are members of interacting binaries that can shed their outer envelopes by Roche-lobe overflow also leading to bright SNIb,c events. That hypothesis was considered in Ref. 16. That is, a fraction  $f_b$  of all massive stars in the range of (8 to 40)  $M_{\odot}$  could result in bright SNIb,c via binary interaction.

## 2.2. Failed supernovae

It is usually presumed<sup>40</sup> that all single massive stars with progenitor masses with  $M>25~M_{\odot}$  end their lives as fSNe. However, this cutoff is uncertain. For single stars above this cutoff mass, the whole star collapses leading to a black hole and no detectable SNe. Allowing for a fraction  $f_b\sim25\%$  of stars with M=(25–40)  $M_{\odot}$  to form SNIb,c by binary interaction, then the rate for fSNe is given by, <sup>16</sup>

$$R(\text{fSN}) = (1 - f_b)\psi_*(z) \times \frac{\int_{25 \ M_{\odot}}^{40 \ M_{\odot}} dM \phi(M)}{\int_{M_{\min}}^{M_{\max}} dM \ M \phi(M)} + \psi_*(z) \times \frac{\int_{40 \ M_{\odot}}^{125 \ M_{\odot}} dM \phi(M)}{\int_{M_{\min}}^{M_{\max}} dM \ M \phi(M)}.$$
(4)

There appears to be a nonmonotonic dependence of the success of the explosion on progenitor mass.<sup>44–47</sup> These numerical investigations suggest that the compactness of the progenitor core just prior to collapse is a good indicator of the success of the explosion, although the onset of SN turbulence may be a better indicator.<sup>47</sup> A correct estimate of the relic neutrino background should include segmented ranges for fSNe and successful SNe in the range from 10 to 25  $M_{\odot}$ .

## 2.3. ONeMg supernovae

ONeMg (or electron-capture) SNe involve explosion energies and optical luminosities that are an order of magnitude less than normal CCSNe, although they provide some contribution to the SRN. Hence, they may go undetected. ONeMg SNe are believed to arise from progenitor masses in the range of 8  $M_{\odot} \leq M \leq$  10  $M_{\odot}$ . Such SNe occur<sup>48</sup> when an electron-degenerate ONeMg core reaches a critical density (at  $M_{\rm core} \sim 1.4~M_{\odot}$ ). In this case, the electron Fermi energy exceeds the threshold for electron capture on <sup>24</sup>Mg. These electron captures cause a loss of hydrostatic support from the electrons and also a heating of the material. Ultimately, this leads to a dynamical collapse and the ignition of an O-Ne-Mg burning front that consumes the star.

## 2.4. Star formation rate

The cosmic SFR  $\psi_*(z)$  is key component of theoretical estimates of the SRN background. Determining the SFR is an involved procedure <sup>16,18,35</sup> based upon different sources, e.g. ultraviolet (UV) light from galaxies and the far infrared (FIR) luminosity. <sup>49</sup> It also depends <sup>51</sup> upon modeling fits to the SED. Uncertainties from this procedure were analyzed in Refs. 16 and 18. The SFR also depends upon the choice of the stellar IMF.

It was noted in Ref. 35 that the measured CCSN rate  $[R_{\rm SN}({\rm Obs})]$  in the redshift range  $0 \le z \le 1$  appears to be about a factor of two smaller than the CCSN rate deduced from the measured<sup>49</sup> cosmic massive-SFR. This is the so-called SN rate problem.<sup>16,35</sup> One possible solution to this involves uncertainty<sup>16</sup> in the inferred SN rate out to redshift  $z \sim 1$ . Another possible explanation is from the uncertainty in the lower mass limit for the progenitors of CCSNe.<sup>17</sup>

A commonly adopted form for a fit to the SFR is the Madau formula<sup>49</sup> given by:

$$\psi_*(z) = \frac{a(1+z)^b}{1 + [(1+z)/d]^c} M_{\odot} \text{ yr}^{-1} \text{ Mpc}^{-3},$$
 (5)

where a = 0.015, b = 2.7, c = 5.6, and d = 2.9.

Another convenient functional form for the SFR is conveniently parametrized as a continuous piecewise linear fit to the observed SFR versus redshift.<sup>34</sup>

$$\psi_*(z) = \dot{\rho_0} \left[ (1+z)^{\alpha\eta} + \left(\frac{1+z}{B}\right)^{\beta\eta} + \left(\frac{1+z}{C}\right)^{\gamma\eta} \right]^{\frac{1}{\eta}}.$$
 (6)

Parameters adopted in Refs. 34 and 35 are  $\dot{\rho_0} = 0.016 \ h_{73}^3 \ M_{\odot} \ \mathrm{Mpc}^{-3} \ \mathrm{yr}^{-1}$  for the cosmic SFR at z=0, as well as the parametrization  $\alpha=3.4,\ \beta=-0.3,$  and  $\gamma=-3.5$ . Breaks at  $z_1=1$  and  $z_2=4$  are smoothed with  $\eta=-10$ , and the normalization is  $B=(1-z_1)^{-\alpha/\beta}=5000$  and  $C=(1+z_1)^{(\beta-\alpha)/\gamma}(1+z_2)^{1-\beta/\gamma}=9$ . A somewhat different parametrization was deduced in Ref. 16 based upon different

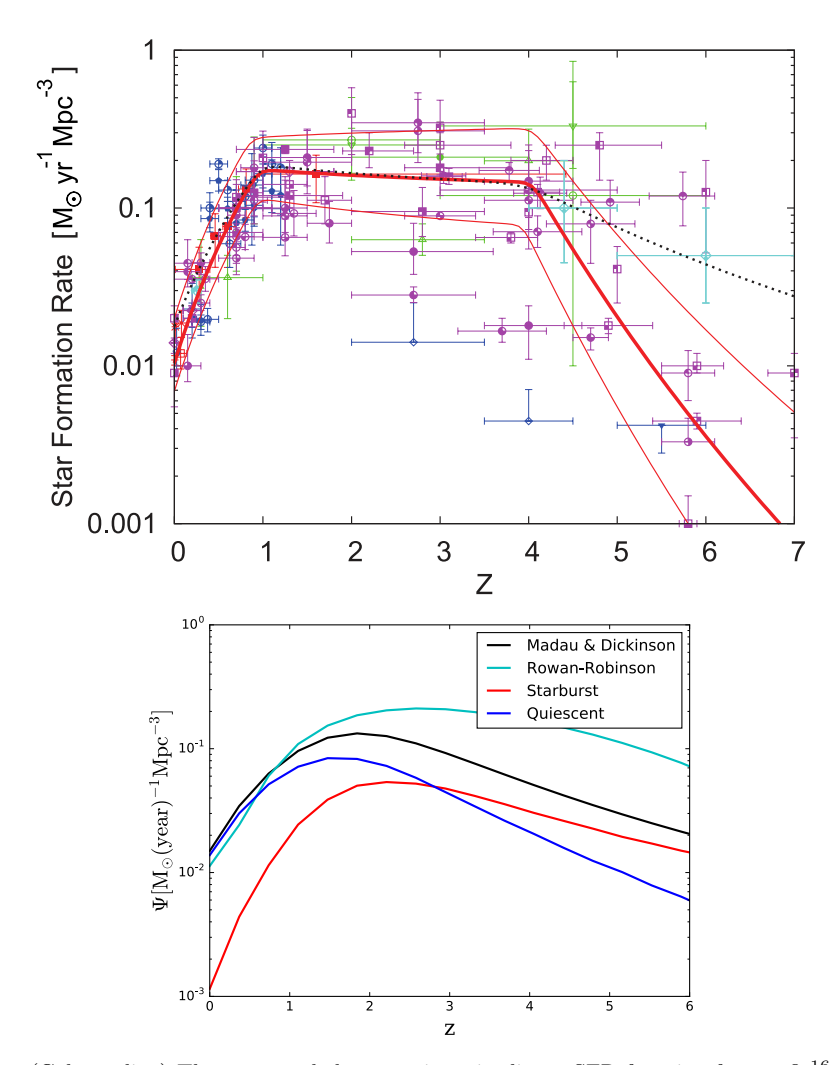


Fig. 2. (Color online) The top panel shows a piecewise linear SFR function from a fit<sup>16</sup> to the subset of observed dust-corrected data. Red, blue, magenta, light blue, and green points show the observed data in IR, optical, UV, X-ray/ $\gamma$ -ray, and radio bands, respectively. Red lines show the SFR as function of redshift z deduced from  $\chi^2$  fitting, along with the  $\pm 1\sigma$  upper and lower limits to the SFR. The reduced  $\chi^2_r$  for the fit is 2.3. The black dotted line shows the SFR at high redshift proposed in Yüksel  $et~al.^{34}$  The bottom panel from Hidaka  $et~al.^{18}$  illustrates the uncertainty in the SFR from various parametrizations. The black line is the commonly adopted Madau SFR. <sup>49</sup> The cyan line shows the SFR of Ref. 52. For illustration the figure also includes possible additional starburst (red) and quiescent (blue) components as suggested by Lacey  $et~al.^{50}$ 

data at low redshift. The piecewise fit from Ref. 16 is illustrated in the upper panel of Fig. 2. The fit from Ref. 34 is shown by the dotted line.

As an illustration of the overall uncertainty in the derived SFR the bottom panel of Fig. 2 (from Hidaka *et al.*<sup>18</sup>) shows the SFR from various parametrizations. The black line is the commonly adopted Madau parametrization<sup>49</sup> of Eq. (5). The

cyan line shows the SFR of Rowan and Robinson.<sup>52</sup> For illustration the figure also includes possible additional starburst (red) and quiescent (blue) components as suggested by Lacey et al.<sup>50</sup> The effects of these additions to the SFR were explored in Ref. 18 and found to be not particularly important for determining the SRN spectrum. The reason for this<sup>16</sup> is because the observed relic SN neutrino spectrum is mainly determined by the SFR for  $z \le 1$ . Although the SFRs at high redshift can deviate by more than an order of magnitude, the overall uncertainty in the relic SN neutrino spectrum due to the SFR remains less than a factor of 2.<sup>16</sup>

Most evaluations of the SFR are based upon the UV luminosity that is mainly due to OB stars. The dust surrounding galaxies, however, always complicates the evaluation of the UV luminosity. There is a claim that the SFR based upon UV light is underestimated especially for starburst galaxies. <sup>52</sup> A method based upon SED modeling has been proposed <sup>52</sup> that takes into account the star formation embedded in dense molecular clouds. This study indicated that the SFR for z > 3.5 is higher by a factor of 2 to 3 than the estimate from UV light. Effects of this were analyzed in Ref. 18.

In Ref. 16, three different versions of the SFRs were studied as a means to estimate the overall uncertainty in the SFR dependence. One was a revised SFR based upon a piecewise linear fit to the observed SFR versus redshift. They also considered SFR models<sup>53</sup> with and without corrections for dust extinction.

# 2.5. Initial mass function $\phi(M)$

A convincing theory for the universal IMF has not yet been established. One of the remaining uncertainties is the metallicity dependence of the IMF. In Ref. 18 the dependence of the detected neutrino spectrum on a metallicity-dependent IMF and other changes in the IMF were analyzed. A broken power-law<sup>54</sup> Salpeter A IMF (Sal-A) is often assumed,

$$\phi(M) = M^{-\zeta},\tag{7}$$

with  $\zeta = 2.35$  for stars with  $M \ge 0.5~M_{\odot}$  and  $\zeta = 1.5$  for  $0.1~M_{\odot} < M < 0.5~M_{\odot}$ .

Most of the popular IMFs including the Sal-A are observationally deduced for stars in the Milky Way. There are also theoretical derivations of the power-law index for the IMF. For example, a power law IMF is explained by the turbulent motion of molecular clouds in a magnetic field. $^{55}$ 

The relationship between metallicity and the IMF has also been considered in Ref. 18. The IMF in metal poor environments could favor higher mass stars because molecular clouds may not sufficiently cool to allow gravitational collapse on small scales. Reference 18 explored the IMF-metallicity relationship by adopting a cosmological metallicity evolution. This was based upon observational evidence  $^{56}$  that IMF evolution occurs in low-z galaxies for which the IMF-metallicity relationship obeys

$$\zeta = 2.2 (\pm 0.1) + 3.1 (\pm 0.5) \times [M/H]. \tag{8}$$

Metallicity evolution is closely related with galaxy evolution. However, both the stellar and gas phase metallicity must be accurately considered. Reference 57 studied the galaxy mass-metallicity relation based upon cosmological zoom-in simulations that include gas inflow and outflow to estimate the metallicity evolution accurately. They found  $[M/H] = 0.4[\log(M_*/M_{\odot}) - 10] + 0.67 \exp(-0.50z) - 1.04$ , where  $M_*$  is the galactic stellar mass. For the metallicity of the gas phase, it was found that  $[M/H] = 0.35[\log(M_*/M_{\odot}) - 10] + 0.93 \exp(-0.43z) - 1.05$ . In addition, galactic mass evolution is expected, and the average of  $M_*$  depends upon the redshift z. The galaxy cosmological mass function can be expressed as  $\langle M_* \rangle = 10^{11}(1+z)^{-0.58}[M_{\odot}]$ . These two studies have been used to deduce the cosmic metallicity evolution and to determine that a z-dependent IMF has a small effect on the observed SRN.

# 3. Source Neutrino Spectrum $(dN_{\nu}^{SN}(E_{\nu}')/dE_{\nu}')$

## 3.1. Neutrino spectra

The uncertainty due to variations of estimates of the emergent neutrino spectra from CCSNe was analyzed in Ref. 16. It is usually assumed  $^{16,34}$  that the dependence on progenitor mass is small compared to the uncertainty in the neutrino temperatures themselves. The reason for this is that the mass of most observed neutron star SN remnants is rather narrowly constrained  $^{59}$  to be  $\sim 1.4~M_{\odot}$ . This narrow range of observed remnant neutron star masses suggests that the associated neutrino temperatures should also be tightly constrained. Hence, it is reasonable to adopt a SN 1987A model (i.e. progenitor mass  $\simeq 16.2~M_{\odot}$ , remnant mass  $\simeq 1.4~M_{\odot}$ , liberated binding energy  $^{60} \simeq 3.0 \times 10^{53}$  erg). Nevertheless, an evaluation of the validity of the assumption that this SN1987A model is representative of every corecollapse SN with progenitor masses in the range of 8 to 25  $M_{\odot}$  and also every SNIb,c over the mass range of 8–40  $M_{\odot}$  in any of the possible paradigms needs to be done.

The liberated binding energy is divided roughly equally among the six neutrino species (three flavors and their antiparticles). The neutrino spectra can be roughly approximated by a Fermi-Dirac distribution with temperatures and chemical potentials determined from fits to the numerically determined neutrino transport.

One can characterize the emergent neutrino spectra by the average neutrino energies (or temperatures and chemical potential) in time. Even in the context of a single progenitor model, however, it was noted in Ref. 16 that a range of predicted neutrino temperatures and chemical potentials are obtained from various SN corecollapse simulations in the literature. Nevertheless, for most models the fitted chemical potential is small and can be neglected. It was concluded <sup>16</sup> that the uncertainty ( $\sim \pm 50\%$ ) in the neutrino temperatures constituted one of the largest uncertainties in the expected relic neutrino detection rate. However, a recent survey <sup>61</sup> of modern SN collapse simulations all tend to predict lower uniform neutrino energies and/or temperatures. However, deviations were noted at late times.

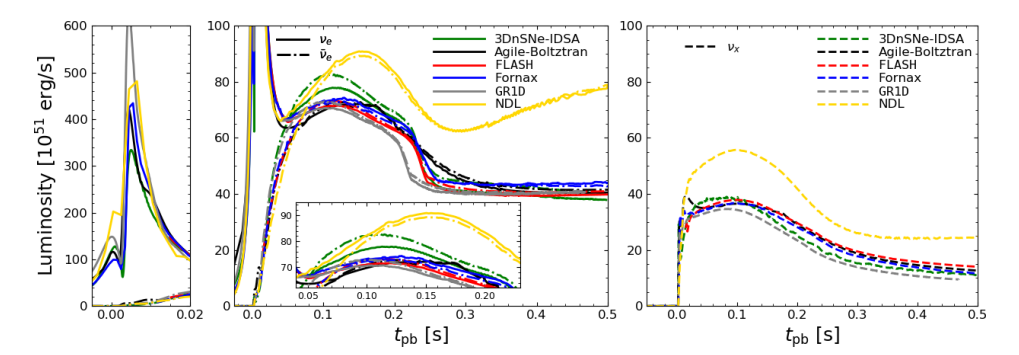


Fig. 3. Comparison of neutrino luminosity light curves predicted by various CCSN codes in the literature. <sup>61</sup> There is remarkable agreement among most codes except the NDL prediction. This relates to the use of more extensive <sup>82</sup> neutrino opacities in the newer codes as described in the text.

## 3.2. Neutrino luminosities

The emergent neutrino spectra can be integrated to obtain the total luminosities of each flavor over time. Figure 3 shows a comparison of a benchmark study with a number of modern spherical 1D SN codes<sup>61</sup> plus our own results based upon the older general relativistic Wilson (NDL) code.<sup>63,64</sup>

Figure 3 shows that there is now remarkable similarity among the neutrino luminosities for all of the modern codes except for the older CCSN models like the NDL.<sup>63,64</sup> This difference can be traced<sup>81</sup> to the use of better neutrino interaction rates<sup>82</sup> in the newer codes. Specifically, the NDL code makes use of a simpler formulation of neutrino opacities as described in Refs. 62, 63 and 83, whereas the convergence of the newer CCSN codes shown on Fig. 3 is based upon a more recent set of neutrino opacities.<sup>61</sup> Scattering and absorption on free nucleons and heavy nuclei along with electron neutrino absorption on nuclei, inelastic neutrino-electron scattering, and electron-positron annihilation are from Ref. 84. Other neutrino effects include weak magnetism, recoil corrections, <sup>85</sup> ion-ion correlations, <sup>86</sup> corrections for the nuclear form factor<sup>87,88</sup> and nucleon-nucleon Bremsstrahlung. <sup>89</sup> In Ref. 81, it was shown that in large part, the increase in the opacity due to neutrino-nucleon scattering could account for the difference between the NDL and newer codes.

Moreover, in Ref. 91 neutrino luminosities were generated for 97 separately derived equations of state that satisfy nuclear and neutron star constraints. There is good convergence of the luminosities for all equations of state, but the average neutrino energies begin to diverge after about 1 s. Overall, the convergence of the neutrino opacities and equations of state suggest that there is less temperature uncertainty in the SRN spectrum than was deduced in Ref. 16.

## 4. SRN Detection Rate

A Hyper-Kamiokande next-generation Čerenkov detector has been proposed, <sup>29,30</sup> consisting of a megaton of pure water laden with 0.1–0.2% GdCl<sub>3</sub> to enhance the

neutron tagging efficiency and reduce the background.<sup>3</sup> The detected SRN energy spectrum in such a detector can be written as:

$$\frac{dN_{\text{event}}}{dE_{e^+}} = N_{\text{target}} \cdot \varepsilon(E_{\nu}) \cdot \frac{1}{c} \cdot \frac{dF_{\nu}}{dE_{\nu}} \cdot \sigma(E_{\nu}) \cdot \frac{dE_{\nu}}{dE_{e^+}}$$
(9)

where  $N_{\rm target}$  is the number of target particles in the water Čerenkov detector,  $\varepsilon(E_{\nu})$  is the efficiency for neutrino detection,  $dF_{\nu}/dE_{\nu}$  is the incident flux of SRNs, and  $\sigma(E_{\nu})$  is the cross section for neutrino absorption:  $\bar{\nu}_e + p \rightarrow e^+ + n$ , and  $E_{\nu} = E_{e^+} + 1.3$  MeV for the neutron proton mass difference. For simplicity one can set  $\varepsilon(E_{\nu}) = 1.0$ , and use the cross-sections given in Ref. 65 when calculating the reaction rate of the SRN with detector target material.

One only needs to consider the detection of  $\bar{\nu}_e$ , because the cross-section in a water Čerenkov detector for the  $\bar{\nu}_e + p \to e^+ + n$  reaction is about  $10^2$  times larger than that for  $\nu_e$  detection via  $\nu_e + n \to e^- + p$ . The threshold detection energy for SRN is  $\sim 10$  MeV due to the existence of background  $\bar{\nu}_e$  emitted from terrestrial nuclear reactors. An upper detection limit is  $\sim 30$  to 40 MeV due to the existence of noise from the atmospheric  $\bar{\nu}_e$  background.

An illustration of the detector SRN spectrum from Ref. 18 is shown in Fig. 4. This shows the anticipated number of events after 10 years run time. The vertical gray-shaded region below 10 MeV illustrates the background due to terrestrial reactors. The lower gray-shaded region indicates the expected background noise due to atmospheric neutrinos. The red-shaded bands indicate the uncertainty in the predicted neutrino signal from the uncertainty in the SFR and the detector statistics. It was suggested in Ref. 18 that the largest uncertainty may be due to different models for the EoS for fSNe. The upper pink band is for a relatively stiff fiducial EoS,<sup>67</sup> while the lower green band is the spectrum for a fiducial soft EoS.<sup>66</sup>

## 4.1. Nuclear EoS uncertainty

The results shown in Fig. 4 and the EoS uncertainty deduced in Refs. 16–18 are based upon the effects of two extreme equations of state. One is the very soft Thomas–Fermi plus Liquid Drop Model EoS of Lattimer and Swesty<sup>66</sup> (for a nuclear compression modulus of K=180). The other is the rather stiff Relativistic Mean Field (RMF) 1998 model Shen *et al.*<sup>67</sup> These were chosen because these represented extreme examples of available calculations of the neutrino spectra from both CCSNe and fSNe.<sup>68,69</sup>

It should be noted, however, that there are now more stringent observational limits on the EoS than when those two formulations were developed. For one, there are now firm determinations  $^{70,71}$  of binary neutron star systems for which a neutron star mass as large a  $2.01\pm0.04~M_{\odot}$  is obtained. The More recently, the mass of a neutron star in the MSP J0740+6620 system was measured to be  $2.17^{+0.11}_{-0.10}~M_{\odot}$ . Such large neutron star masses cannot be achieved with an EoS as soft as that of the Lattimer & Swesty (K=180) formulation.

Moreover, another important development is the observation by the LIGO and VIRGO Scientific collaboration of gravity waves from the binary neutron star merger GW170817.<sup>73</sup> Subsequent analysis<sup>74</sup> in which both stars are required to have the same EoS places strong limits on the tidal polarizability, which in turn depends upon the neutron star radius to the fifth power. Indeed, only an EoS for which the radius of a 1.4  $M_{\odot}$  neutron star is less than 13.3 km is consistent with the 90% confidence limit. A separate analysis<sup>75</sup> of neutron star atmospheres concludes that the neutron star radius must be less than about 12.5 km. Such compact stars, however, are incompatible with the stiff 1998 RMF Shen EoS. Hence, the large uncertainty due the EoS indicated in Fig. 4 is an overestimate of the EoS uncertainty.

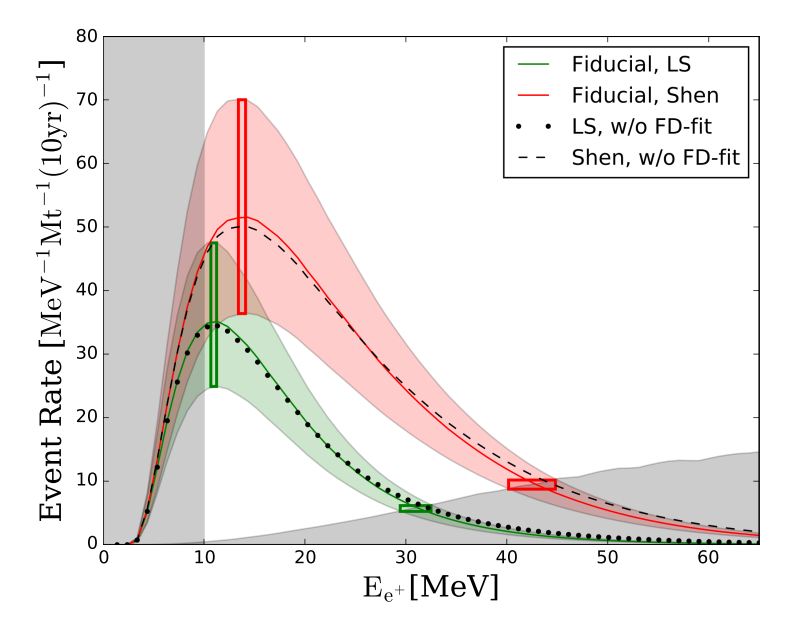


Fig. 4. (Color online) Predicted  $e^+$  energy spectra and uncertainties  $^{17}$  in the total SRN detections for the case of no neutrino oscillations. The uncertainty bands are based upon the dispersion in the observed cosmic SFR and the detector statistics. The results for two different fSNe models based upon a stiff Fiducial Shen  $^{67}$  EoS (red line) and a soft Fiducial LS EoS  $^{66}$  (green line). The dashed and dotted lines illustrate the uncertainty in using a FD fit to the spectra rather than the numerical spectra. The gray-shaded energy range below 10 MeV indicates the region where the background noise due to reactor  $\bar{\nu}_e$  may dominate. The shaded energy range that intersects the spectrum at  $\sim 30$ –46 MeV indicates the region where the background may be dominated by noise from atmospheric neutrinos. Rectangular regions represent the peak of the spectrum and the locations where the neutrino signals overwhelm the atmospheric neutrino noise.

Indeed, the set of equations of state that can satisfy both the neutron star maximum mass constraint and the neutron star radius constraint is rather limited.<sup>74</sup> This implies that there is probably less EoS uncertainty on the relic neutrino spectrum than that deduced in Refs. 16–18. Indeed, a new analysis of the uncer-

tainties in the observed relic neutrino spectrum is warranted based upon these constraints.

As an illustration, Fig. 5 shows a new series of calculations<sup>81</sup> of the emergent electron neutrino spectrum from a set of EoSs<sup>66,77–79</sup> that are mostly consistent with the neutron star maximum mass requirement. Calculations were run with the modern fully general-relativistic spherically symmetric open -source code GR1D.<sup>80</sup> Neutrino luminosities were computed using the open-source library NuLib.<sup>82</sup> The progenitor is the 20  ${\rm M}_{\odot}$  star calculated by Woosley and Heger.<sup>90</sup> Note that HShen refers to the 2011 version of the RMF EoS<sup>77</sup> not the 1998 version used in Refs. 16–18. Similarly,, LS220 denotes the compression modulus K=220 version of the Lattimer and Swesty 1991 EoS, not the K=180 version used previously.<sup>16–18</sup> Here, one can see that there is less uncertainty in the source luminosity from the newer equations of state that satisfy the neutron star maximum mass constraint. However, the LS220 and HShen equations of state keep the neutrino luminosity high for longer times. A similar conclusion has been obtained in Ref. 91 for the same progenitor and GR1D CCSN model, but for 97 new Skyrme parametrized EoSs all of which satisfy observational constraints, yet show very little dispersion in the neutrino spectra.

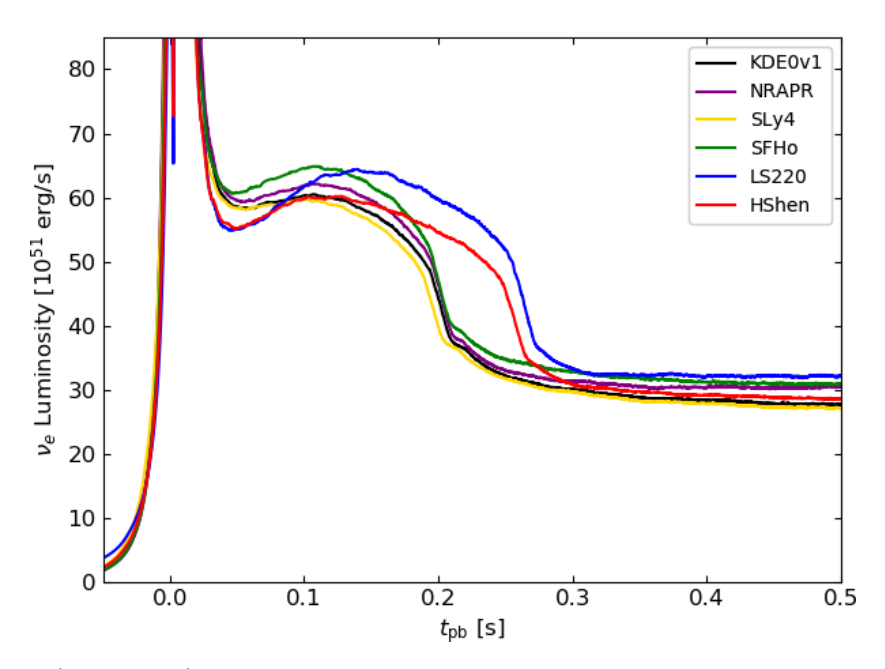


Fig. 5. (Color online) Neutrino luminosity vs. time post bounce  $t_pb$  for various equations of state. The simulations were run using the open-source, spherically symmetric, general relativistic hydrodynamic code GR1D, <sup>80</sup> and the neutrino opacities were obtained using the open-source library NuLib. <sup>82</sup> The progenitor is the 20  $M_{\odot}$  star calculated by Woosley and Heger. <sup>90</sup> The black, purple and yellow curves are the three Skyrme models from Schneider *et al.* (2017)<sup>79</sup> that satisfy the 2  $M_{\odot}$  constraint for cold neutron stars. The green curve is the SFHo EoS from Hempel *et al.* (2012); <sup>92</sup> the blue curve is the EoS from Lattimer and Swesty (1991), <sup>66</sup> for an incompressibility modulus of 220 MeV; the red curve is the EoS from Shen (2011). <sup>77</sup>

# 4.2. Dependence on neutrino oscillations

It is known that the flavor eigenstates for the neutrino are not identical to the mass eigenstates. The flavor eigenstates  $\nu_e$ ,  $\nu_\mu$ ,  $\nu_\tau$  are related to the mass eigenstates by a unitary matrix U:

$$\begin{pmatrix} \nu_e \\ \nu_\mu \\ \nu_\tau \end{pmatrix} = U \begin{pmatrix} \nu_1 \\ \nu_2 \\ \nu_3 \end{pmatrix}, \tag{10}$$

where the matrix U can be decomposed as:

$$U = \begin{pmatrix} U_{e1} & U_{e2} & U_{e3} \\ U_{\mu 1} & U_{\mu 2} & U_{\mu 3} \\ U_{\tau 1} & U_{\tau 2} & U_{\tau 3} \end{pmatrix}$$
(11)

$$\equiv \begin{pmatrix} 1 & 0 & 0 \\ 0 & c_{23} & s_{23} \\ 0 & -s_{23} & c_{23} \end{pmatrix} \begin{pmatrix} c_{13} & 0 & s_{13}e^{-i\delta} \\ 0 & 1 & 0 \\ -s_{13}e^{i\delta} & 0 & c_{13} \end{pmatrix} \begin{pmatrix} c_{12} & s_{12} & 0 \\ -s_{12} & c_{12} & 0 \\ 0 & 0 & 1 \end{pmatrix}.$$
(12)

Here,  $s_{ij} \equiv \sin \theta_{ij}$ ,  $c_{ij} \equiv \cos \theta_{ij}$ , and  $\theta_{ij}$  is the mixing angle between neutrinos with mass eigenstates i and j, and  $\delta = [0, 2\pi]$  is the Dirac charge-parity (CP) violating phase.

For the mixing of mass eigenstates one must consider two cases: (1) the normal mass hierarchy,  $m_1 < m_2 < m_3$ ; and (2) the inverted mass hierarchy,  $m_3 < m_1 < m_2$ . Both models have two resonance density regions. The resonance at higher density is called the H-resonance, and the one at lower density is called the L-resonance. In the normal mass hierarchy, both resonances are in the neutrino sector. In the inverted mass hierarchy, however, one resonance is in the neutrino sector, while the other is in the antineutrino sector.

The prospects for detecting effects of neutrino flavor oscillations in the spectrum of detected SRNs has been discussed<sup>14</sup> using a parametrized form for the emitted neutrino spectrum from Ref. 93, and also in Ref. 13 using the SN simulations of the Basel group.<sup>94</sup> In Refs. 16–18 the limit of three neutrino oscillation paradigms were considered according to Ref. 95.

If one assumes an efficient conversion probability  $P_H$  of  $\bar{\nu}_3 \leftrightarrow \bar{\nu}_1$  at the H-resonance in the inverted hierarchy, then the  $\bar{\nu}_e$  flux emitted from CCSNe becomes:<sup>16</sup>

$$\phi_{\bar{\nu}_e} = |U_{e1}|^2 \phi_{\bar{\nu}_1} + |U_{e2}|^2 \phi_{\bar{\nu}_2} + |U_{e3}|^2 \phi_{\bar{\nu}_3}$$

$$= |U_{e1}|^2 \{ (1 - P_H) \phi_{\bar{\nu}_1}(0) + P_H \phi_{\bar{\nu}_3}(0) \}$$

$$+ |U_{e2}|^2 \phi_{\bar{\nu}_2}(0) + |U_{e3}|^2 \{ P_H \phi_{\bar{\nu}_1}(0) + (1 - P_H) \phi_{\bar{\nu}_3}(0) \}.$$
(13)

From this, one can deduce the survival probability  $\bar{P}$  for  $\bar{\nu}_e$ :

$$\bar{P} = |U_{e1}|^2 P_H + |U_{e3}|^2 (1 - P_H) \approx 0.7 P_H. \tag{14}$$

The same result occurs for the normal mass hierarchy. Hence, one can define this case of complete non-adiabatic mixing as:

$$\bar{\nu}_e(0) \to 0.7 \times \bar{\nu}_e^0 + 0.3 \times \nu_x^0$$
 (Case I). (15)

It is now known<sup>96</sup> that the  $\theta_{13}$  mixing is relatively large  $[\sin^2(\theta_{13}) = 0.092 \pm 0.0016 \, (\text{stat}) \pm 0.005 \, (\text{syst})]$ . Thus, if there is no SN shock, then the survival probability can be small  $(P_H \to 0)$  so that the conversion of  $\bar{\nu}_e$  into  $\nu_x$  is efficient. One can define<sup>16</sup> this situation of complete adiabatic mixing in the inverted neutrino mass hierarchy as:

$$\bar{\nu}_e(0) \to \nu_x^0$$
 (Case II). (16)

The case with no neutrino oscillations is adopted as Case III in Refs. 16–18.

Figure 6 illustrates the calculated <sup>16</sup> dependence of detection event rates on the three oscillation scenarios. These results are similar to those of other studies. <sup>9,11–13</sup> Shaded bands show uncertainties from the SFR and detector statistics.

The calculated<sup>16</sup> positron detection rate in Fig. 6 shows the effect of the three different neutrino oscillation scenarios for a stiff RMF<sup>67</sup> EoS. Here, one can see that the main effect of the neutrino oscillations is on the amplitude of the detected signal. Whereas the EoS affects not only the amplitude but also the energy of the

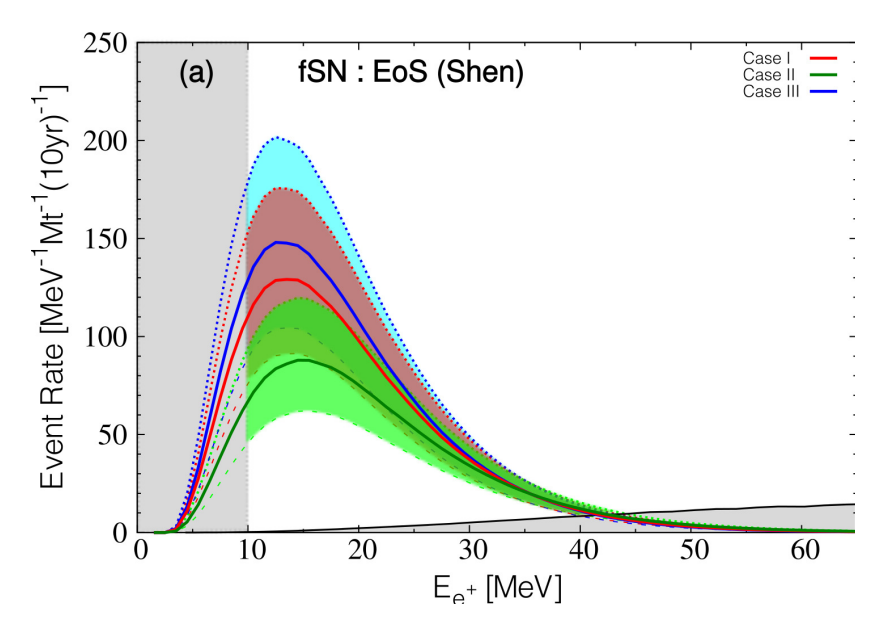


Fig. 6. (Color online) Effects of neutrino oscillations on the predicted  $^{16}$   $e^+$  energy spectra as a function of  $e^+$  energy for a  $10^6$  ton water Čerenkov detector with 10 years of run time. Red, green, and blue lines shows the SRN detection rate in the case of nonadiabatic (Case I), adiabatic (Case II), or the no neutrino oscillations (Case III), respectively, for the case of a stiff RMF<sup>67</sup> EoS.

peak as shown in Fig. 4. Thus, it may be possible to distinguish the oscillation effect from the EoS uncertainty especially as the SFR uncertainty diminishes.

# 4.3. Dependence of SRN detection on the neutrino self-interaction effect

In the case of an inverted mass hierarchy, a "self-interaction effect" among neutrinos<sup>97</sup> might cause an additional difference between the detected energy spectrum of SN neutrinos.<sup>13</sup> The possible importance of this effect was calculated in Ref. 16 for the simplest case of single-angle neutrino self-interaction.

A single angle interaction  $^{97}$  causes the energy spectra of  $\bar{\nu}_e$  and  $\nu_x$  ( $\bar{\nu}_\mu$  and  $\bar{\nu}_\tau$ ) to exchange with each other at about 4.0 MeV. This means that the energy spectra of  $\bar{\nu}_e$  and  $\nu_x$  are perfectly exchanged in the discernable energy range of water Čerenkov detectors. Hence, a neutrino self-interaction could change the SRN energy spectrum in oscillation Case II into that of Case III. See however, Ref. 20 for a review of neutrino self-interactions, and the possibility that multi angle effects suppress flavor conversions.

Figure 7 from Ref. 16 shows that for the most part the correction for neutrino self-interaction produces a slight increase in the high energy end of the detected neutrino spectrum. More recently, it has been demonstrated that the combined effects of neutrino oscillations and neutrino self-interaction can have a dramatic effect on the emergent neutrino spectrum. Such effects may be discernable in the detected SNR spectrum and warrant further study.

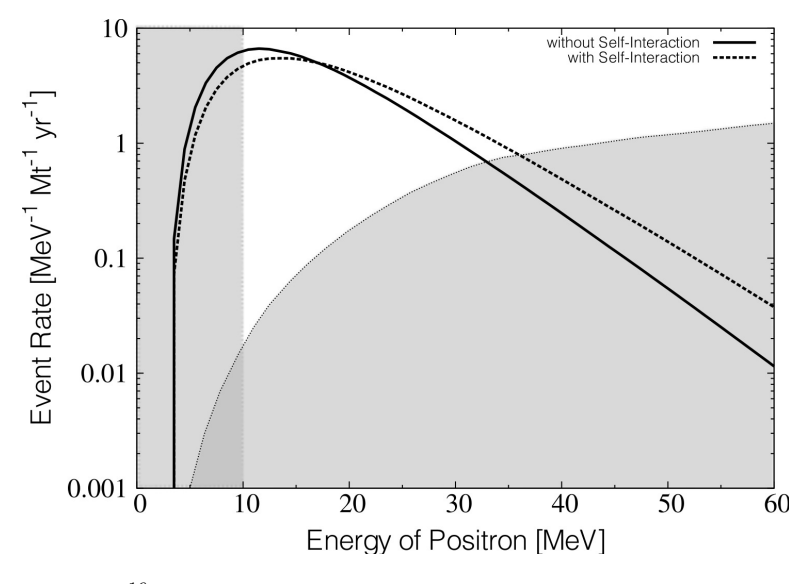


Fig. 7. Calculation <sup>16</sup> of the detected SRN energy spectrum cases with (dashed line) or without (solid line) a single-angle neutrino self-interaction. Shaded regions are the backgrounds as defined in Fig. 4.

# 5. Conclusions

The essential results of the past studies in Refs. 16–18 of the uncertainties in the predicted SRN spectrum are summarized on Figs. 8 and 9. These works have considered a wide variety of astrophysical scenarios and investigated the EoS dependence of the SRN spectrum for each case with and without the occurrence of neutrino oscillations. It was consistently found that the EoS dependence of the SRN spectrum manifests prominently in the high energy peak and tail in any scenario considered. The robustness of this EoS dependence can be understood in that the SRN spectrum is determined mostly by the SFR for z < 2, so that cosmological effects and metallicity-dependent effects at high redshift have a negligible effect. However, as noted above, this EoS dependence needs to be reevaluated in the context of the current stringent observational constraints on the possible equations of state.

Figure 8 shows<sup>18</sup> rectangles indicating the location of the peak and tail of the detected SRN for a variety of astrophysical conditions and the two equations of state in Fig. 4. On this figure, the Fiducial case is the parametrized Madau<sup>49</sup> SFR, with

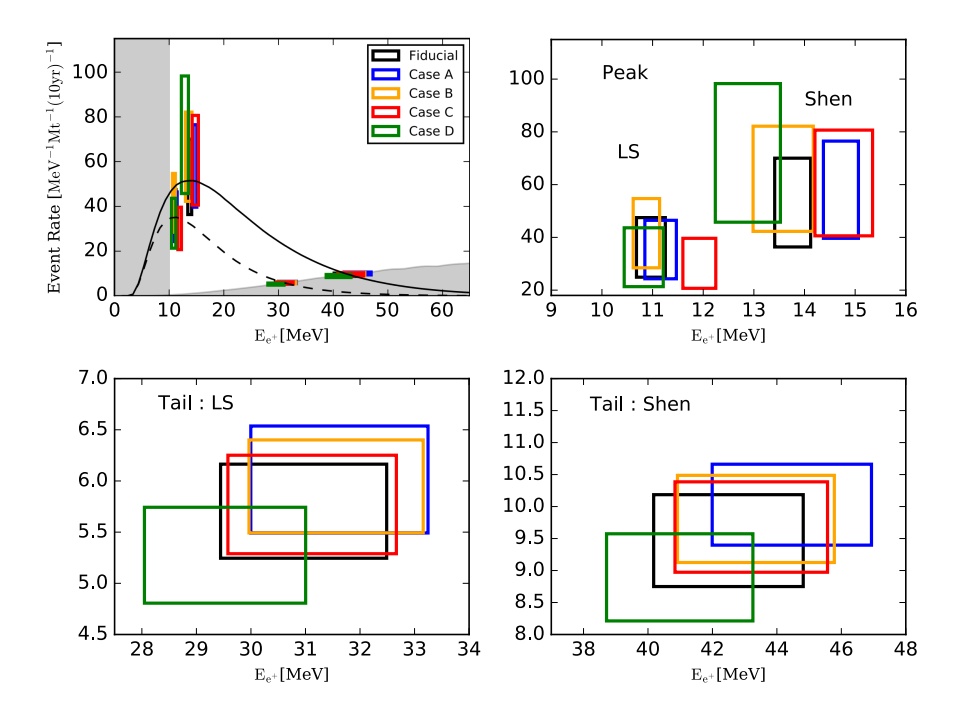


Fig. 8. Rectangles indicating the location of peak and tail, which characterize the spectrum for each cases. For reference, the left upper panel shows the spectrum of the fiducial case without the uncertainty bands included. The solid line is for the Shen EoS and the dashed line for the soft LS. The right upper panel shows the detail of the peak locations for both the Shen and LS EoSs. Similarly, the details of tails are shown in the left bottom (for the LS EoS) and right bottom panel (for the Shen EoS). In spite of the many uncertainties, there is a unique dependence on the EoS that may be discernable in the SNR detector signal.

no neutrino oscillations; Case A is a revised SFR that omits lower-mass progenitors as a means to solve the red supergiant problem;<sup>36</sup> Case B includes the Sarburst and Quiescent SFR shown on Fig. 4; Case C includes a metallicity-dependent variable IMF; and Case D includes a SFR enhanced at high-z. In that paper<sup>18</sup> it was concluded that the EoS sensitivity is strong enough to differentiate the EoS during CCSNe and fSNe. However, as noted above, new constraints on the EoS may preclude this sensitivity as the soft EoS is now ruled out.

Figure 9 illustrates how the neutrino temperature  $T_{\nu}$  in CCSNe explosions can affect the detected spectra. In particular, the neutrino temperature influences the value of the positron energy that gives the maximum event rate, i.e.  $E_{\rm peak}$ . A measurement of the ratio of the number of events at  $E_{\rm peak}$  compared to the events at higher energy (say 25 MeV) might be used to directly infer the neutrino temperature emerging from SNe. The different points on this plot represent a subset of nine points sampling the concordance region of the compendium of 30 models published from 1987 to 2012 and listed in Table 4 of Ref. 16. These temperatures were used to infer the  $\bar{\nu}_e$  spectra and associated detector signal. We note that the most recent models suggest lower neutrino temperatures and may be associated with a steeply declinir

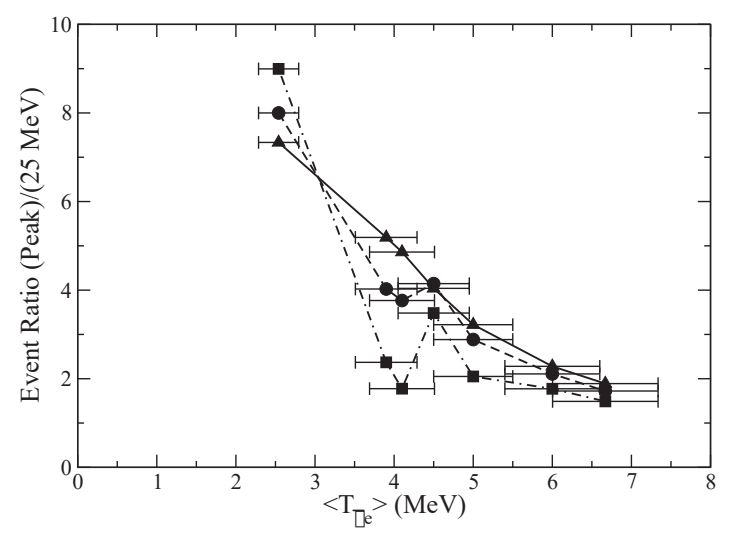


Fig. 9. Sensitivity or the ratio of events at the observed positron peak to events with a positron energy of 25 MeV, corresponding to nine fiducial SN neutrino temperatures and different neutrino oscillation conditions adopted from the compendium of models in Mathews et al. <sup>16</sup> Circles and dashed line are for the case of neutrino oscillations with complete nonadiabatic mixing. Squares and dot-dashed line are for the case of adiabatic mixing in the an inverted mass hierarchy. Triangles and the solid line are for the case of no neutrino oscillations. These points illustrates how the observed positron spectrum might be used to directly infer the supernova electron anti-neutrino temperature. Error bars drawn indicate the adopted 10% uncertainty in model neutrino temperatures. The vertical scatter in the points indicates the uncertainty due to neutrino oscillation scenarios.

## Acknowledgments

Work at the University of Notre Dame (G.J.M.) supported by the U.S. Department of Energy under Nuclear Theory Grant DE-FG02-95-ER40934. This work was also supported in part by Grants-in-Aid for Scientific Research of JSPS (15H03665, 17K05459) of the Ministry of Education, Culture, Sports, Science, and Technology of Japan.

## References

- 1. D. H. Hartmann and S. E. Woosley, Astropart. Phys. 7, 137 (1997).
- 2. T. Totani, K. Sato and Y. Yoshida, Astrophys. J. 460, 303 (1996).
- 3. J. F. Beacom and M. R. Vagins, Phys. Rev. Lett. 93, 171101 (2004).
- 4. J. F. Beacom and L. E. Strigari, Phys. Rev. C 73, 5807 (2006).
- 5. J. F. Beacom, Ann. Rev. Nucl. Part. Sci. 60, 439 (2010).
- 6. H. Yüksel and J. F. Beacom, Phys. Rev. D 76, 083007 (2007).
- 7. S. Horiuchi et al., Phys. Rev. D 79, 0830138 (2009).
- 8. C. Lunardini and A. Yu. Smirnov, J. Cosmol. Astropart. Phys. 06, 009 (2003).
- 9. C. Lunardini, Phys. Rev. Lett. 102, 231101 (2009).
- 10. C. Lunardini, arXiv:1007.3252.
- L. Yang and C. Lunardini, Phys. Rev. D 84, 063002 (2011).
- 12. J. Keehn and C. Lunardini, Phys. Rev. D 85, 043011 (2012).
- 13. C. Lunardini and I. Tamborra, J. Cosmol. Astropart. Phys. 07, 012 (2012).
- 14. S. Chakraborty, S. Choubey and K. Kar, *Phys. Lett. B* **702**, 209 (2011).
- 15. K. Nakazato, Phys. Rev. D 88, 083012 (2013).
- G. J. Mathews, J. Hidaka, T. Kajino and J. Suzuki, Astrophys. J. 790, 115 (2014).
- J. Hidaka, T. Kajino and G. J. Mathews, Astrophys. J. 827, 85 (2016).
- J. Hidaka, T. Kajino and G. J. Mathews, Astrophys. J. 869, 31 (2018).
- 19. K. Nakazato, E. Mochida, Y. Niino and H. Suzuki, Astrophys. J. 804, 75 (2015).
- 20. A. Mirizzi et al., Rivista del Nuovo Cimento 39, 1 (2016).
- 21. H. Wei, Z. Wang and S. Chen, Phys. Lett. B 769, 255 (2017).
- 22. J. Barranco, A. Bernal and D. Delepine, J. Phys. G 45, 055201 (1918).
- 23. S. Anandagoda, D. Hartmann, M. Ajello and A. Desai, Res. Notes AAS 4, 4 (2020).
- 24. K. Kyutoku and K. Kashiyama, Phys. Rev. D 97, 103001 (2018).
- T. S. H. Schilbach, O. L. Caballero and G. C. McLaughlin, *Phys. Rev. D* 100, 043008 (2019).
- 26. Z. Lin and C. Lunardini, Phys. Rev. D 101, 023016 (2020).
- 27. A. Hopkins and J. Beacom, Astrophys. J. 651, 142 (2006).
- 28. S. Shashank, I. Tamborra and M. Bustamante, arXiv:1912.09115 [astri-pj.HE].
- 29. Hyper-Kamiokande Working Group (K. Abe et al.), arXiv:1109.3262 [hep-ex].
- Super-Kamiokande Collab. (Y. Takeuchi et al.), Nucl. Instrum. Methods 952, 161634 (2020).
- 31. Super-Kamiokande Collab. (K. Bayes et al.), Phys. Rev. D 85, 052007 (2012).
- 32. H. Sekiya, Nucl. Phys. B 237, 111 (2013).
- 33. L. Strigari et al., J. Cosmol. Astropart. Phys. **04**, 017 (2005).
- 34. H. Yüksel et al., Astrophys. J. 683, L5 (2008).
- 35. S. Horiuchi et al., Astrophys. J. 738, 154 (2011).
- 36. S. J. Smartt, Ann. Rev. Astron. Astrophys. 47, 63 (2009).
- S. J. Smartt, J. J. Eldridge, R. M. Crockett and J. R. Maund, Mon. Not. R. Astron. Soc. 395, 1409 (2009).

- 38. S. J. Smartt, Proc. Astr. Soc. Pac. 32, 16 (2015).
- T. Sukhbold, T. Ertl, S. E. Woosley, J. M. Brown and H.-T. Janka, *Astrophys. J.* 821, 38 (2016).
- 40. A. Heger et al., Astrophys. J. 591, 288 (2003).
- 41. C. L. Fryer, S. E. Woosley and D. E. Hartmann, Astrophys. J. 526, 152 (1999).
- 42. P. Podsiadlowski, P. C. Joss and J. J. Hsu, Astrophys. J. 391, 246 (1992).
- 43. K. Nomoto, K. Iwamoto and T. Suzuki, Phys. Rep. 256, 173 (1995).
- 44. M. Ugliano, H.-T. Janka, A. Marek and A. Arcones, Astrophys. J. 757, 69 (2012).
- 45. O. Pejcha and T. A. Thompson, Astrophys. J. 801, 90 (2015).
- T. Sukhbold, T. Ertl, S. E. Woosley, J. M. Brown and H.-T. Janka, *Astrophys. J.* 821, 38 (2016).
- 47. S. M. Couch, M. L. Warren and E. P. O'Connor, Astrophys. J. 890, 127 (2020).
- 48. J. Isern, R. Canal and L. Labay, Astrophys. J. **372**, L83 (1991).
- 49. P. Madau and M. Dickinson, Annu. Rev. Astron. Astrophys. 52, 415 (2014).
- 50. C. G. Lacey et al., Mon. Not. R. Astron. Soc. 462, 3854 (2016).
- 51. C. Conroy and P. G. van Dokkum, Astrophys. J. 760, 71 (2012).
- 52. M. Rowan-Robinson et al., Mon. Not. R. Astron. Soc. 461, 1100 (2016).
- 53. C. Kobayashi et al., Astrophys. J. 539, 26 (2000).
- 54. I. K. Baldry and K. Glazebrook, Astrophys. J. 593, 258 (2003).
- 55. P. Padoan and A. Nordlund, Astrophys. J. **576**, 870 (2002).
- I. Marton-Navarro, J. P. Brodie, R. C. E. van den Bosch, A. J. Romanowsky and D. A. Forbes, Astrophys. J. 832, L11 (2016).
- 57. X. Ma et al., Mon. Not. R. Astron. Soc. 456, 2140 (2016).
- A. R. Lopes, A. Iribarrem, M. B. Ribeiro and W. R. Stoeger, Astron. Astrophys. 572, A27 (2014).
- 59. J. M. Lattimer, Ann. Rev. Nucl. Part. Sci. 62, 485 (2012).
- 60. D. Arnett et al., Annu. Rev. Astron. Astrophys. 27, 629 (1989).
- 61. E. O'Connor et al., J. Phys. G 45, 104001 (2018).
- 62. R. Mayle et al., Astrophys. J. 318, 288 (1987).
- J. R. Wilson and G. J. Mathews, J. R. Wilson and G. J. Mathews, Relativistic Numerical Hydrodynamics (Cambridge Univ. Press, 2003).
- 64. J. P. Olson et al., arXiv:1612.08992.
- 65. A. Strumia and F. Vissani, Phys. Lett. B 564, 42 (2003).
- 66. J. Lattimer and F. D. Swesty, Nucl. Phys. A 535, 331 (1991).
- 67. H. Shen et al., Nucl. Phys. A 637, 435 (1998).
- 68. K. Sumiyoshi et al., Astrophys. J. 629, 922 (2005).
- 69. K. Sumiyoshi et al., Astrophys. J. 688, 1176 (2008).
- P. B. Demorest, T. Pennucci, S. M. Ransom, M. S. E. Roberts and J. W. T. Hessels, Nature 467, 1081 (2010).
- 71. J. Antoniadis et al., Science **340**, 448 (2013).
- 72. H. T. Cromartie et al., arXiv:1904.06759.
- LIGO and Virgo Scientific Collabs. (B. P. Abbot et al.), Phys. Rev. Lett. 119, 161101 (2017).
- 74. LIGO and Virgo Scientific Collabs. (B. P. Abbot et al.), Phys. Rev. Lett. 121, 161101 (2018).
- 75. A. W. Steiner, J. M. Lattimer and E. F. Brown, Astrophys. J. **722**, 33 (2010).
- 76. L. Boccioli, G. J. Mathews and E. O'Connor, Astrophys. J., submitted (2019).
- 77. H. Shen, H. Toki, K. Oyamatsu and K. Sumiyoshi, Astrophys. J. 197, 20 (2011).
- 78. A. W. Steiner, J. M. Hempel and T. Fischer, Astrophys. J. 774, 17 (2013).
- A. S. Schneider, L. F. Roberts and C. D. Ott, Phys. Rev. C 96, 065802 (2017).

- 80. E. O'Connor and C. D. Ott, Class. Quantum Grav. 27, 114103 (2010).
- L. Boccioli, G. J. Mathews, M. Warren, I. Suh and M. Correa, Bull. Am Phys. Soc. T08.008 (2019).
- 82. E. O'Connor, Astrophys. J. Suppl. Ser. 219, 24 (2015).
- 83. N. Itoh, Progr. Theor. Phys. 54, 1580 (1975).
- 84. S. W. Bruenn, Astrophys. J. Suppl. Ser. 58, 771 (1985).
- 85. C. J. Horowitz, *Phys. Rev. D* **65**, 043001 (2002).
- 86. C. J. Horowitz, Phys. Rev. D 55, 4577 (1997).
- 87. S. W. Bruenn and A. Mezzacappa, Phys. Rev. D 56, 7529 (1997).
- 88. M. Rampp and H.-T. Janka, Astron. Astrophys. J. 396, 361 (2002).
- 89. S. Hannestad and G. Raffelt, Astrophys. J. 507, 339 (1998).
- 90. S. E. Woosley and A. Heger, Phys. Rep. 442, 269 (2007).
- 91. A. S. Schneider, L. F. Roberts, C. D. Ott and E. O'Connor, arXiv:1906.02009.
- M. Hempel, T. Fischer, J. Schaffner-Bielich and M. Liebendörfer, Astrophys. J. 748, 70 (2012).
- 93. M. T. Keil, G. G. Raffelt and H.-T. Janka, Astrophys. J. 590, 971 (2003).
- 94. T. Fischer et al., Astron. Astrophys. 517, A80 (2010).
- 95. A. S. Dighe and A. Y. Smirnov, Phys. Rev. D 62, 3007 (2000).
- 96. Daya Bay Collab. (F. P. An et al.), Phys. Rev. Lett. 108, 171803 (2012).
- 97. G. Fogli et al., J. Cosmol. Astropart. Phys. 12, 010 (2007).
- 98. H. Ko et al., Astrophys. J. Lett. 891, L24 (2020).